Available online at www.sciencedirect.com

SCIENCE DIRECT®

Thermochimica Acta 439 (2005) 110–118

thermochimica acta

www.elsevier.com/locate/tca

Heat-flow patterns in Tian–Calvet microcalorimeters: Conductive, convective, and radiative transport in gas dosing experiments

Luis Enrique Vilchiz, Arturo Pacheco-Vega, Brent E. Handy*

CIEP-Facultad de Ciencias Químicas, Universidad Autónoma de San Luis Potosí, Av. Dr. Manuel Nava 6,
Zona Universitaria, CP 78210, San Luis Potosí, SLP, Mexico

Received 23 June 2005; received in revised form 14 September 2005; accepted 19 September 2005

Abstract

Mathematical models of a Tian–Calvet microcalorimeter were solved numerically by the finite-element method in an effort to understand the relative importance of the three basic heat transfer mechanisms operative during gas dosing experiments typically used to determine heats of adsorption on catalysts and adsorbents. The analysis pays particular attention to the quantitative release of heat through various elements of the cell and sensor cups to assess time delays and the degree of thermal shunting that may result in inaccuracies in calorimetric measurements. Conductive transfer predominates in situations where there is high gas headspace pressure. The convection currents that arise when dosing with considerable gas pressure in the cell headspace region are not sufficiently strong to shunt significant amounts of sample heat away from being sensed by the surrounding thermopiles. Therefore, the heat capture fraction (heat sensed/heat produced) does not vary significantly with gas headspace pressure. During gas dosing under very low gas headspace pressure, radiation losses from the top of the sample bed may significantly affect the heat capture fraction, leading to underestimations of adsorption heats, unless the heat radiated from the top of the catalyst bed is effectively reflected back to the sample region or absorbed by an inert packing layer also in thermal contact with the thermopile wall.

Keywords: Tian–Calvet calorimeter; Calibration; Adsorption; Finite-element analysis

---

1. Introduction

Amongst the three basic types of calorimeter systems, the heat conduction, or Tian–Calvet calorimeter is most suited for studying the relatively slow thermal process associated with gas adsorption in isothermal microcalorimetry [1,2]. At the core of the Tian–Calvet calorimeter is a sample holder that for practical reasons is partially surrounded by a thermally conducting wall embedded with thermocouples to sense the temperature difference generated between the sample holder and a heat sink that is ideally maintained at a constant temperature. The thermal characteristics necessary in constructing a useful core unit are straightforward, namely, deliver the unknown sample heat signal as efficiently and perhaps as rapidly as possible to the heat-flux transducers and insure that the transducer elements deliver this heat flow to a sinking element held perfectly isothermal. However, putting this concept into practice is complicated by the details of the experiment. In the specific case of isothermal gas–solid adsorption calorimetry, the sample must be preconditioned with various temperature treatments and gas environments, evacuated, and gas doses introduced in a controlled manner onto the catalyst surface. This requires a connection tube for gas transfer, with the result that some of the sample heat emission will be shunted away from the heat-flux sensing elements.

Design aspects of Tian–Calvet microcalorimeters for gas adsorption studies have been detailed by Parillo and Gorte [3]. In general, one can try to channel the heat emissions toward the sensing element wall, although conductive heat transfer between sample and sensing wall is hindered by the low thermal conductivities of the powdered sample bed, sample cell wall (quartz), heat transfer grease or filler between cell and thermopile wall. It is thus not realistic to expect to capture and sense all of the sample heat emissions. More importantly, accurate calibration of heat signal requires that the heat transfer flow pattern of the calibration test be identical to that prevailing during an experiment

---

* Corresponding author. Tel.: +52 444 826 2440/811 8102;
fax: +52 444 826 2372.
E-mail address: handy@uaslp.mx (B.E. Handy).

0040-6031/$ – see front matter © 2005 Elsevier B.V. All rights reserved.
doi:10.1016/j.tca.2005.09.014

Nomenclature

c_{s}	specific heat of solid component (J/kg K)
e_ϕ	unit vector in ϕ-direction
g	gravitational constant (m/s^2)
h_{ext}	external heat transfer coefficient (W/m^2 K)
p	local pressure (Pa)
$\dot{q}$	heat generation (W/m^3)
Q_{sense}	heat sensed by thermocouples (W)
Q_{source}	heat generated by the sample (W)
r, ϕ, z	cylindrical coordinates
R_{H}	heat capture fraction
t	time (s)
T	fluid temperature (K)
T_∞	reference fluid temperature (K)
T_{c}	surface temperature of cell (K)
T_{ext}	external ambient temperature (K)
$\hat{T}$	temperature within solid component (K)
$\mathbf{u}$	fluid velocity vector (m/s)
u_r, u_ϕ, u_z	fluid velocity components (m/s)

Greek symbols

α	fluid thermal diffusivity (m^2/s)
α_{s}	thermal diffusivity of solid component (m^2/s)
β	volume expansivity (K^{-1})
∇	Nabla operator
ν	kinematic viscosity (m^2/s)
ρ	fluid density (kg/m^3)
ρ_{s}	density of solid component (kg/m^3)

Subscript

i	index for ith solid component

with adsorbent [4]. Two kinds of calibrations may be performed, i.e., calibration by Joule effect probe, or by a “chemical” calibration with a catalyst sample of known heat yield. The former case has the advantage of simplicity and precision in applying a known energy pulse to the system. But without a valid heat transfer model, it is difficult to assess whether the degree of thermal shunting with the Joule effect probe is the same as with the adsorbent cell, because of differences in cell/probe geometry and thermal properties. On the other hand, the “chemical” calibration will display similar heat transfer characteristics as the samples of unknown heat yield, yet there are few samples available that demonstrate a precise heat yield with confidence. Calibration must be both precise and accurate when quantifying unknown heat yields. If one wishes additionally to quantify the thermokinetics of a process, knowledge of the characteristic time response of the system is required. While the thermal characteristics of the calorimeter itself may not vary over time or with experiment, the same cannot be said for the sample cell and its contents. In gas adsorption calorimetry of catalysts and adsorbents, the sample is usually a poor heat conductor, being a porous ceramic type material. As a result, the heat signal may be considerably retarded from its point of emission to ultimate detection in the heat-flow sensors. Thermal transport within the cell is also hindered and complicated in gas dosing experiments with very low ($\leq 10^{-1}$ Pa) gas equilibrium pressures. This is especially true when titrating strong adsorption sites, which often represent the most important sites to characterize in a catalyst or adsorbent.

In this work we develop a realistic mathematical model of the central (core) region of a Tian–Calvet microcalorimeter used in our laboratory for gas–solid adsorption studies. The model is used to simulate the heat flow patterns one expects to observe during a typical gas dosing experiment, accounting for conductive and convective heat transfer mechanisms, and to assess the degree of thermal shunting that exists in these experiments. The radiative transfer mechanism is also considered for the case of dosing where the gas pressure is very low.

2. Numerical techniques and mathematical model

The calorimeter being modeled, a schematic of which is illustrated in Fig. 1, is based upon an instrument constructed earlier [5]. The actual calorimeter used a dual-cup sensor core fabricated by International Thermal Instrument Co.[1] The sample and reference cells were constructed of quartz, with 1 mm wall thickness, cell body diameter of 16 mm, and body height (below stem) of 20 mm. Further details on its design are reported in [5]. It is to be noted that, for the simulations, the catalyst powder was usually assumed to have a bed depth of 10 mm, filling half of the cell volume, and to possess thermal properties typical of 1 wt.% Pt/Al_2O_3 [6].

Two different mathematical models of the calorimeter were developed. The first is based on a two-dimensional axisymmetric approach of a single-sensing cup core section formulated to solve the conduction–radiation problem that arises in gas dosing under very low gas headspace pressure. The second is a more comprehensive three-dimensional model of the complete calorimeter (dual sensing cups, core heat sink, heater section and insulation layers in both axial and radial directions) used to study the conjugate conduction–convection heat transfer. To formulate the governing equations for this model, the calorimeter can be divided into three parts: the solid components in which heat generation is present, the solid components without heat generation, and the cell headspace where fluid (dosing gas) exists. Thus, on assuming constant material properties, the applicable equation for each of the solid components is

$$\frac{\partial \hat{T}_i}{\partial t} = \alpha_{\mathrm{s},i} \nabla^2 \hat{T}_i + \frac{\dot{q}}{\rho_{\mathrm{s},i} c_{\mathrm{s},i}}, \tag{1}$$

where $\hat{T}$ is the temperature of the ith solid component, e.g. parts pertinent to the core and sink, as well as the catalyst powder, α_{s} the corresponding thermal diffusivity, $\dot{q}$ the heat generation, ρ_{s} the density of solid component and c_{s} is the specific heat. If there is no heat generation within the solid, then $\dot{q} = 0$ in Eq. (1). For the fluid inside the sensing cup, which is assumed

---

[1] Del Mar, CA, USA.

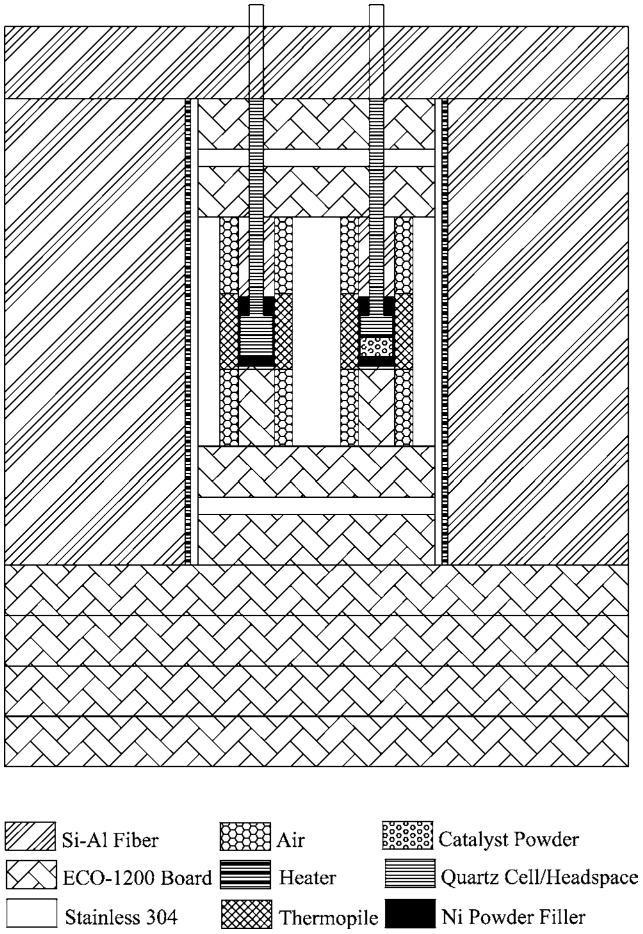

Fig. 1. Schematic of a Tian–Calvet microcalorimeter used for gas adsorption studies.

to be Newtonian, incompressible, with constant properties, the corresponding set of governing equations in the Boussinesq limit for the buoyancy force [7], are

$$\nabla \cdot \mathbf{u} = 0, \tag{2}$$

$$\frac{\partial u}{\partial t} + (\mathbf{u} \cdot \nabla)\mathbf{u} = -\frac{1}{\rho}\nabla p + \nu\nabla^2\mathbf{u} + g\beta(T - T_\infty), \tag{3}$$

$$\frac{\partial T}{\partial t} + (\mathbf{u} \cdot \nabla)T = \alpha\nabla^2 T, \tag{4}$$

where $\mathbf{u}$ represents the velocity vector, p the local pressure, T the temperature of the fluid, T_∞ a reference temperature, ρ, ν, β and α, respectively, the fluid density, kinematic viscosity, volume expansivity, and thermal diffusivity, and g is the gravitational constant.

Due to the fact that both temperature and heat flux for the fluid inside the cell and the solid components in the calorimeter are unknown, they must be determined as part of the solution. As a consequence, Eqs. (1)–(4) represent a fully coupled conjugate heat transfer problem in which conjugacy of the temperature fields for the fluid and the solid components is accomplished by enforcing fluid–solid and solid–solid interfacial continuity of both temperature and heat flux. Thus, heat conduction in the calorimeter must be solved simultaneously with the flow solution for the air inside the cell under the conditions mentioned above.

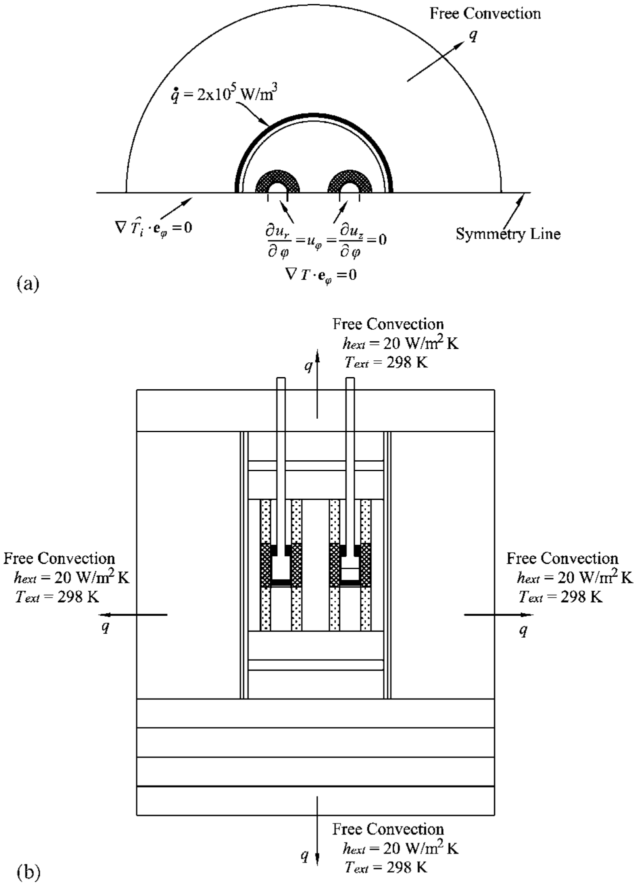

Fig. 2. Boundary and symmetry conditions: (a) side view and (b) top view.

The governing equations for the two problems were discretized and solved using general-purpose software packages based upon the finite-element method. Advantages of employing this method over others, e.g. finite differences and spectral methods, are its flexibility to handle complex geometries, adaptability to set non-uniform grid distributions, and easy specification of boundary conditions on irregular surfaces [8]. The two-dimensional, single-sensor section model was analyzed using FEHT,[2] whereas the full three-dimensional model, in which the gas occupying the cell headspace could also be included, was solved with ANSYS.[3]

Boundary conditions and heat generation terms for the three-dimensional simulations are shown in Fig. 2. Typical values of the external heat transfer coefficient, $h_{\text{ext}} = 20\,\text{W/m}^2\,\text{K}$, and an ambient temperature of $T_{\text{ext}} = 298.15\,\text{K}$ were used. The calorimeter is at an initial temperature of $T_0 = \hat{T}_0 = 298.15\,\text{K}$, and a heat generation term of $\dot{q} = 2 \times 10^5\,\text{W/m}^3$ is considered in the heating elements. Fig. 2 also shows the symmetry boundary conditions applied to reduce the computational domain, and hence, the CPU-time of the computations.

---

[2] http://www.fchart.com.

[3] http://www.ansys.com.

3. Results and discussion

3.1. Experimental heat responses

The calorimeter response to several types of experimental heat signals are shown in Fig. 3. The step change input, generated by constant resistive power from a Joule effect cell, produces essentially a first-order relaxation response, with reference to the Tian equation [2] in which the assumption is uniform temperature within the cell. Higher order terms, due to thermal lags in the cell when the heater is switched on, manifest themselves in the early stage of the response curve, but their presence is minor. The characteristic time constant of the calorimeter, reached at 63.2% of steady-state value, is 375 s. The transducer response signal (ordinate) has been low-pass filtered to remove transients shorter than 4 s, and amplified 1000-fold. With a nominal cup sensitivity of 10 mV/W, a deflection of 1 mV represents 100 μW of continuous power emission from the cell. The calorimetric response to a square energy pulse, Fig. 3(b), of 1200 mJ yield and 120 s duration shows a rapid rise during the heat application period, reaching a maximum power of 2.6 mW about 10 s after the power was removed. The tail region is essentially the relaxation response seen in Fig. 3(a). The heat response profile shown in Fig. 3(c) corresponds to a typical gas dose experiment, whereupon the adiabatic gas uptake was complete over a 2 min period. A peak similar in form to the square energy pulse response is expected, since gas uptake occurred over roughly the same time period. The noticeable difference between the peaks is due to gas adsorption thermokinetics. The gas dose peak achieves maximum 115 s later than the Joule effect pulse, although the total energy yield of both peaks is nearly the same. The time frame of the underlying chemical (adsorption) process occuring in Fig. 3(c) is still shorter than the characteristic time constant of the calorimeter, yet by superimposing one trace on the other, one can try to identify qualitative features of the sample heat emission distinct from the instrument response.

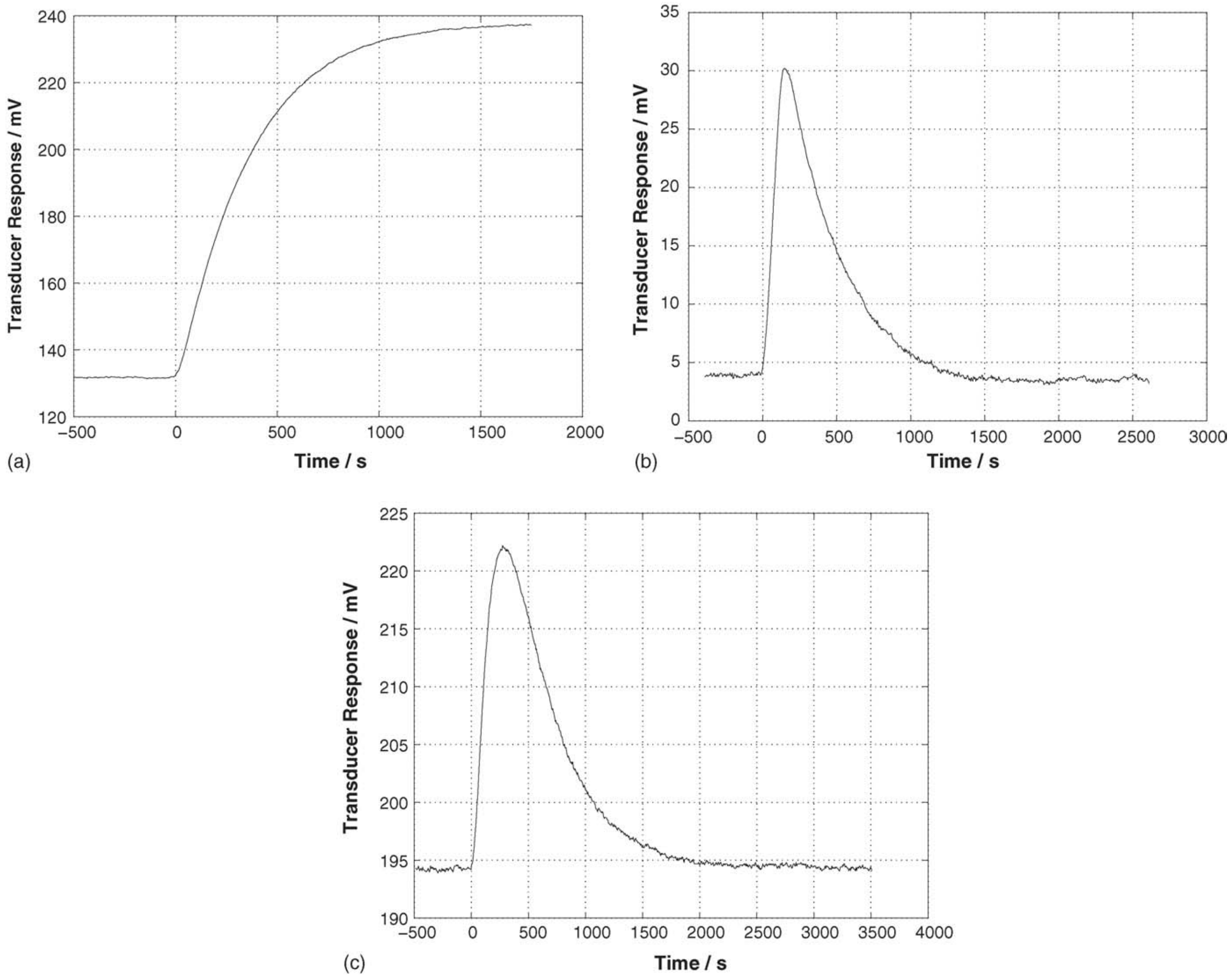

Fig. 3. Calorimetric heat responses: (a) step change response (9.93 mW) from Joule effect probe; (b) heat response to a square energy pulse (9.95 mW, 120 s) from Joule effect probe; (c) heat response from gas dose (heat yield 1.76 J).

3.2. Steady-state temperature distributions

Temperature distributions are shown in Fig. 4(a) and (b) for steady-state operation of the complete calorimeter at a nominal temperature of 503.45 K, obtained by supplying 30 W to a resistance band heater wrapped around the Al shell, modeled here as a thin shell heater element. The maximum temperature variation within the core region, which is composed of quartz cells, thermopiles, and stainless steel heat sink, is 1 K. This variation is primarily axial, with temperature decreasing with vertical position due to differences in the insulation materials used above and below the core. The bottom insulation consists of denser, more conductive fiberboards than the Si–Al fiber blanket that surrounds the heater shell, and is used above the core region. In principle, both sample and reference sensors "see" the same steady-state heat flow pattern, but in practice the heater controller will introduce surges in this heat flow and be a source of noise in the baseline heat response, which may not be completely cancelled out in the difference heat signal. The headspaces of both sample and reference cells are filled with air at 1.33 kPa, simulated as freely convecting, Eqs. (2)–(4), to cell inner walls and to the top of the catalyst bed. Temperature profiles shown in Fig. 4(b) refer to the heat response obtained during a typical gas dosing experiment, whereupon the catalyst bed is generating 23 mW power during a 120 s period. At $t = 120$ s, the catalyst bed temperature is several tenths of a degree higher than its immediate surroundings. Heat transfer may occur by both convection and conduction mechanisms to the headspace gas as well as by conduction through the catalyst bed to the cell walls.

3.3. Fluid flow patterns in the cell headspace

Free convective transport in the cell headspace is more rigorously evaluated by simultaneous solution of the equations of continuity, momentum, and energy conservation, in addition to the heat equations that apply for a strictly heat conduction problem in the solid components. The fluid dynamics of the gas contained within the cell headspace was analyzed in this manner for the calorimeter maintained nominally at 503.45 K as mentioned in the previous section. The no-slip no-penetration conditions, $\mathbf{u} = 0$ $(u_r = u_\phi = u_z = 0)$, were applied to the interior walls of the cell body and stem.

Convection and conduction temperature profiles are shown for the cell body regions in Fig. 5(a) and (b). Fluid flow velocity vectors, represented as arrows whose length is a measure of magnitude are also included. As both figures show, closed convection loops develop in the headspace of each cell. This is due to small lateral temperature differences that exist across the cell walls for any given z-position, since both cells are necessarily arranged off-axis from the geometric center of the calorimeter heat sink. Importantly, the convection loop is mainly localized within the cell body region and implies that only minor amounts of axially directed fluid flow escape upward to the cell stem region. Convection currents did not appear when the simulations

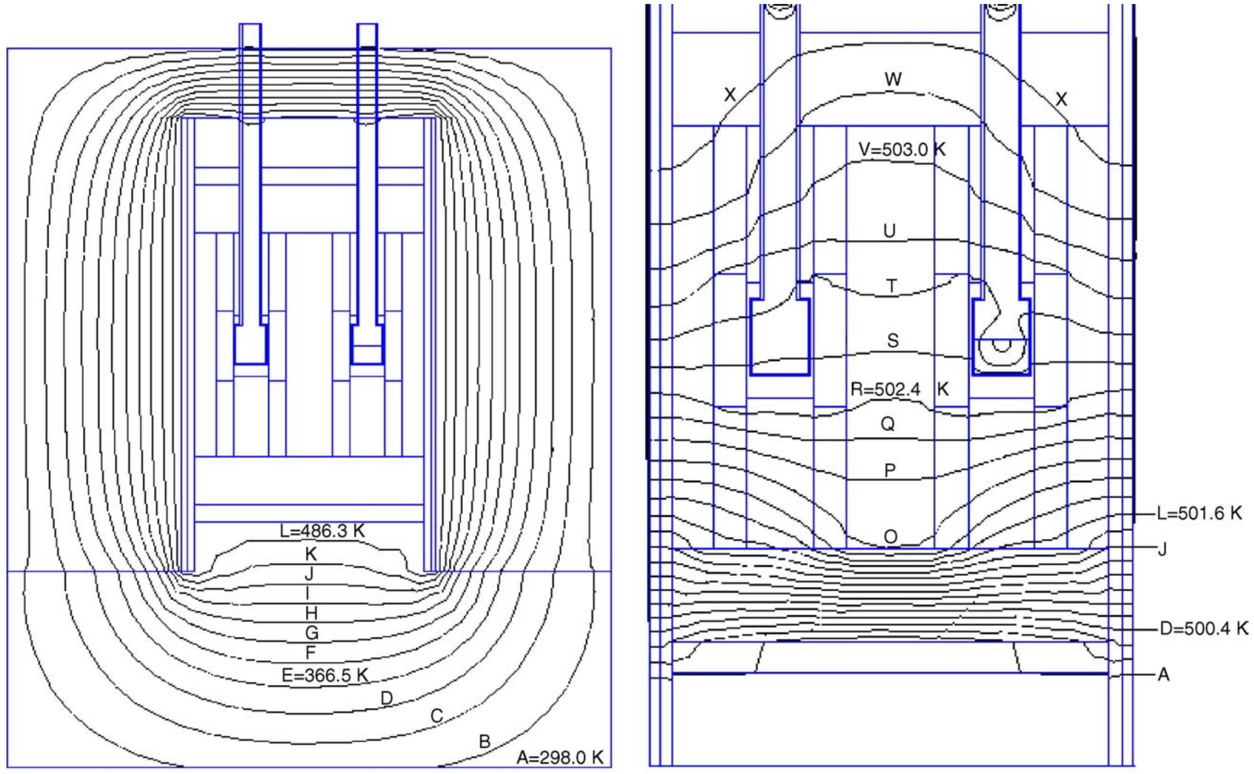

(a) (b)

Fig. 4. Temperature profiles of calorimeter maintained at 503.45 K. (a) Core and heat sink regions. Isotherms, A–L, are in [298, 486.30] K, with 17.12 K intervals. (b) Core region, showing response to catalyst bed heat generation of 23 mW for 120 s (profile shown at $t = 120$ s). Isotherms, A–X, are in [500.40, 503.31] K, with 0.145 K intervals.

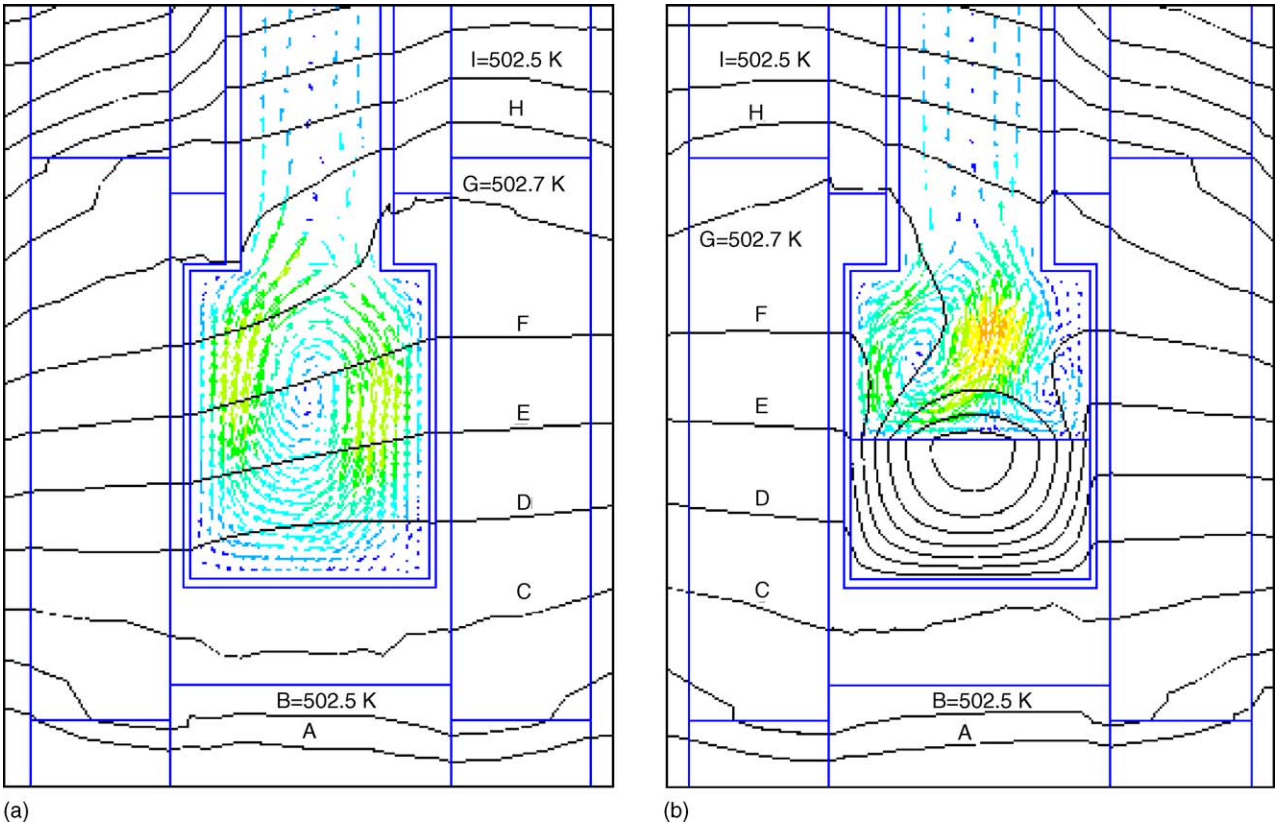

Fig. 5. Velocity and temperature fields in convective–conductive transport within the reference and sample cell region: (a) reference cell and (b) sample cell. Velocities are in the range [0, 0.05] mm/s. Isotherms, A–I, are in the range [502.45, 502.80] K, with 0.05 K intervals.

were run with zero heater power (calorimeter at ambient temperature).

The convection currents in the sample cell headspace are modified by heat generated in the catalyst bed during a gas dose. Heat emission from the bed induces the gas in the headspace to stream upward roughly along the cell central axis, dividing the single, closed convection loop seen with zero sample heat emission into two closed loops. The velocities seen in the sample cell headspace during heat generation are somewhat higher than those registered in the reference cell, but not significantly high enough to change the heat flow mechanisms between sample and reference cells. In fact, the velocity magnitudes are too low to make convective heat transport a significant factor here. The local heat transfer coefficient calculated for any point along the cell wall–gas interface is less than 1 W/m^2 K, which is close to assuming that the wall is adiabatic.

3.4. Temperature profile and heat flow in the cell headspace

The temperature profiles in Figs. 5 and 6 shed some light on the heat flow characteristics of the cells with gas present in the headspace. In the case of the reference cell, the isotherms show nearly linear temperature variation across the cell body (sliced at center), suggesting conductive heat transport being influential through the medium. In the sample cell, heat generation during dosing distorts the isotherms in the gas headspace immediately above the catalyst bed, producing a saddle region showing that the sample heat is largely transported to the cell body walls and not to the stem region above and away from the thermopiles. This demonstrates that sample generated heat is not appreciably shunted away from the sensing thermopiles by either convection or conduction mechanisms. Fig. 6 shows that the temperature profiles are symmetric about the calorimeter axis outside of the cell body regions. Vertical convection currents in the stem sections of each cell arise from buoyancy forces with the fluid rising along the “hotter”-side and falling along the “colder”-side walls. However, as indicated before, the velocities of these currents are very small and will therefore not shunt significant amounts of heat from the cell body regions. Consequently, one can conclude that convection does not play a significant role in heat transfer from the catalyst bed to the sensing thermopiles when there is gas pressure in the cell headspaces.

More important to the issue of calibration in gas adsorption experiments is to determine whether the heat capture fraction, defined as the amount of the total heat generated by the sample that is sensed by the thermopiles, will change with gas dose pressure or with catalyst bed conductivity. If such a pressure effect exists, then the calibration factor would vary with cell equilibrium pressures, giving erroneous results especially for initial heat of adsorption values where the dose equilibrium pressures may be 10 Pa or less. It furthermore implies that differences exist between the heat capture fraction obtained with powder catalyst sample and the value obtained with a Joule effect device.

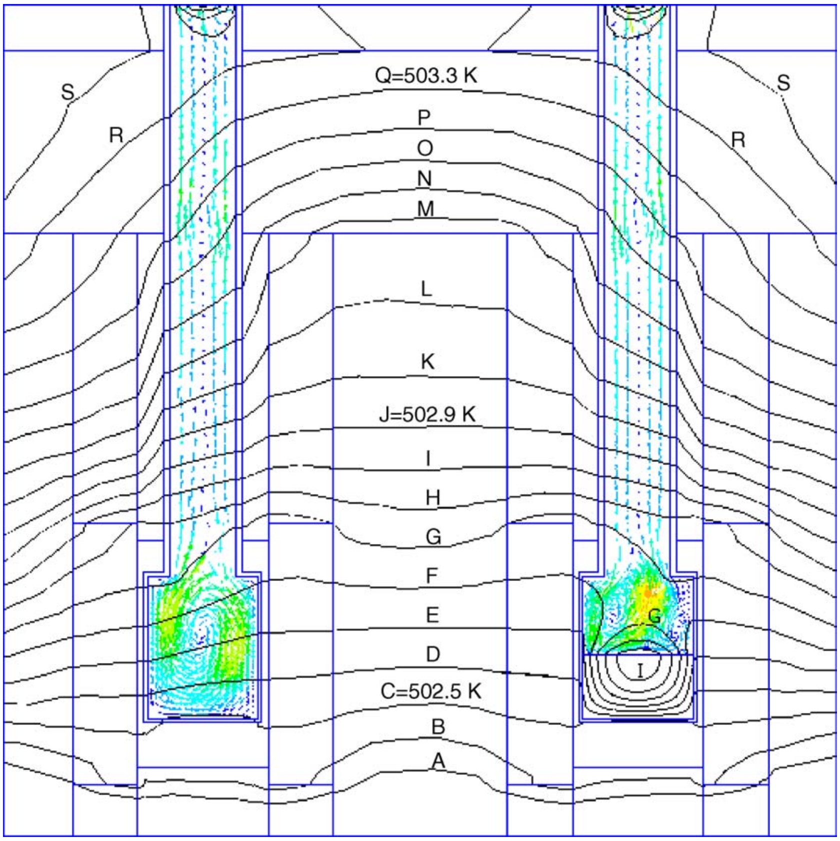

Fig. 6. Temperature field in convective–conductive transport in the overall core region. Isotherms, A–S, are in the range [502.40, 503.35] K, with 0.05 K intervals.

The heat flow response to an energy pulse of size and duration similar to that of a typical gas adsorption dose was simulated by applying a constant power input of 23 mW for 120 s to the catalyst bed element, after which the simulation was continued with zero bed heat emission to observe relaxation of the heat signal response. Heat capture percentages, calculated as

$$R_{\mathrm{H}} = \frac{Q_{\mathrm{sense}}}{Q_{\mathrm{source}}} \times 100, \qquad (5)$$

where Q_{sense} is the heat generated by the sample and Q_{source} is the heat sensed by the thermopiles, are displayed in Table 1. In all cases, thermal shunting amounts to only 4% of the heat generated by the catalyst sample. The highest capture fraction is found for the adiabatic wall case, where the boundary condition for heat flux across the catalyst bed–gas interface is set to zero. The difference between this result and the others shown is due to the small amount of heat generated by the catalyst that transfers to the gas headspace and is shunted away from (not sensed) by the thermopiles. At most, this represents 0.3% of the sample heat emissions and is not significant. Thus, within the framework of the heat conduction–convection transport mechanism, the heat capture fraction does not vary with cell headspace gas pressure. In simulations not shown here, heat capture fractions also do not appear to vary significantly with experimental parameters such as catalyst bed depth or heat pulse profile (power-duration).

3.5. *Gas dosing at very low cell pressure*

Often during the first few doses of gas adsorption calorimetry experiments, when encountering strong adsorption, the gas pressure in the cell headspace remains below 10 Pa throughout the dose. This removes the possibility of heat transfer from catalyst bed to the cell headspace by either conduction or convection mechanisms, but raises the possibility that radiative heat transfer may cause appreciable thermal shunting. Since the strongest adsorption sites are often the most interesting ones to study, it is important to quantify them with some precision.

Simulation results are presented in Fig. 7(a)–(c), using the two-dimensional axi-symmetric single sensing cup model. The model provides similar qualitative results to the more complete three-dimensional model under the conditions described earlier. Based on our analysis of the convection–conduction problem, all inner cell boundaries representing the gas headspace element

Table 1
Simulated heat capture fractions, R_{H}, for gas dosing experiments at different gas headspace pressure and bed-headspace boundary conditions

Bed conductivity (W/m K)	Condition	R_{H} (%)
0.5	Free convection, $p = 1.3$ kPa	96.26
0.5	Free convection, $p = 0.1$ Pa	96.31
0.5	Adiabatic, $p = 0$	96.32
0.5	Pure conduction, $p = 1.3$ kPa	96.32
0.1	Free convection, $p = 1.3$ kPa	95.98

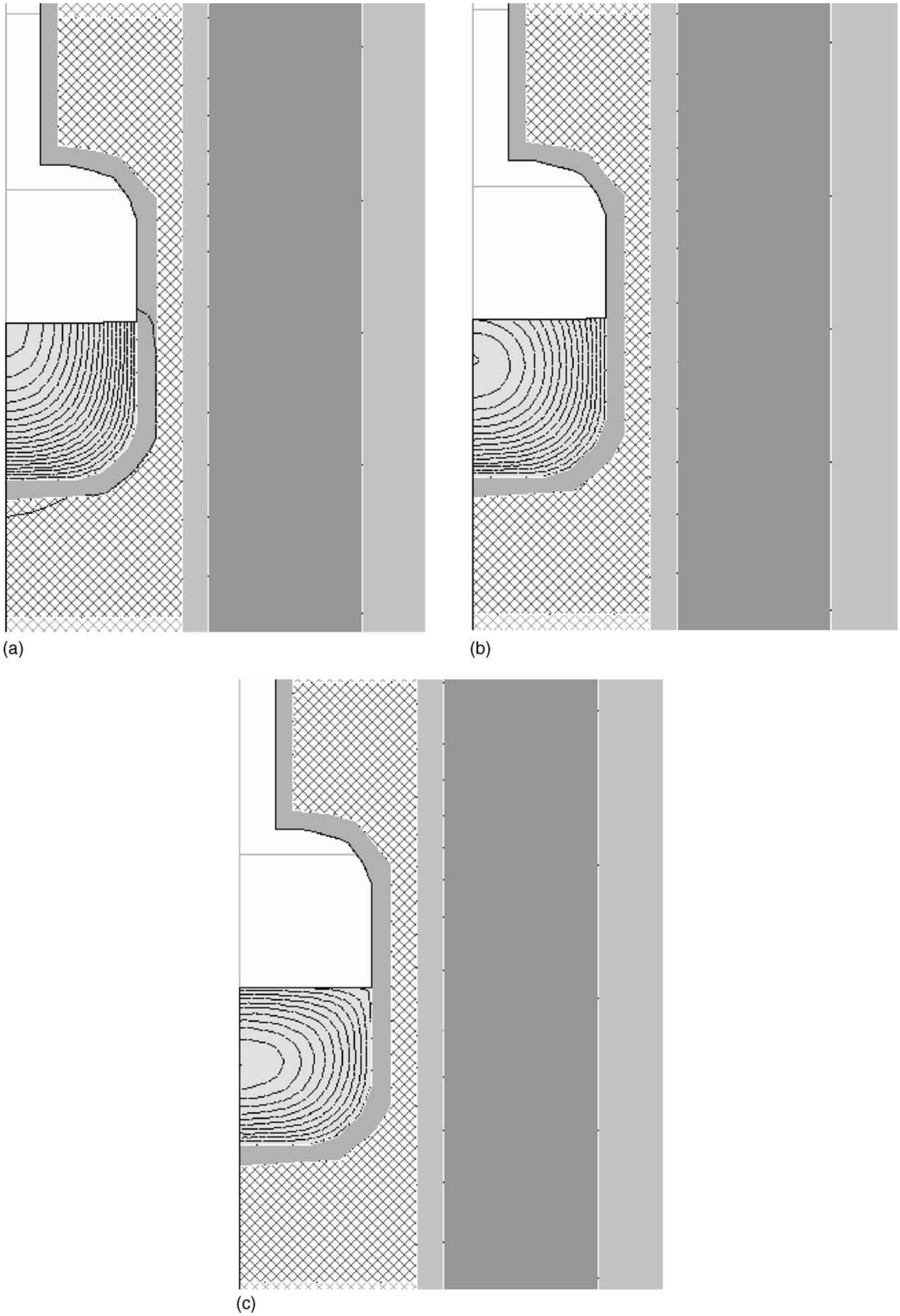

Fig. 7. Simulated temperature distributions in the catalyst bed during dosing under high vacuum with bed/headspace boundary condition: (a) adiabatic, (b) radiative transfer with $T_\mathrm{c} = 298.15\,\mathrm{K}$, and (c) radiative transfer with $T_\mathrm{c} = 770\,\mathrm{K}$.

were made adiabatic. Fig. 7(a) shows temperature profiles within the catalyst bed that is generating 23 mW continuous power. The maximum bed temperature is attained at a point located top center of the bed, and is about 4 K hotter than the surrounding walls ($T_c = 298.15$ K). The heat capture fraction is 86.2%, and is invariant with respect to the other factors probed, such as gas headspace pressure and bed conductivity. Radiative transfer was included by defining an overall heat transfer coefficient in terms of net radiative transfer, using the Stefan–Boltzmann law.

In a worst-case scenario, it is assumed that the top of the catalyst bed will behave as a black body radiator, radiating to surrounding cell inner wall surfaces that maintain 298.15 K at all times, and are non-reflective surfaces. Radiation losses from the top of the bed are evidenced by the lower maximum temperature compared with that in Fig. 7(a), and the acute angles formed by the isotherms at the bed/headspace interface. The heat capture fraction here is 79.7%, almost 8% lower than when radiative transfer is absent. The difference is significant, especially when relying on heat calibrations obtained with Joule effect probe tests where thermal radiation is effectively captured by the surrounding packing material. This 8% difference will of course be minimized by back-reflection from the cell inner walls or by covering the catalyst bed with an IR absorbing material such as inert quartz, as recommended by others [3]. The radiation loss amount will be more pronounced in calorimetry experiments performed at higher temperatures as a consequence of the fourth-power dependency of the Stefan–Boltzmann Law. This is illustrated in Fig. 7(c) where the simulation was re-done with all elements maintained at 770 K. Here the maximum temperature of the bed is 2.5° above surroundings, although the maximum temperature has shifted to a lower position and the heat capture fraction is now only 64.1%.

4. Conclusions

Heat transfer simulations of a Tian–Calvet microcalorimeter led to the following conclusions concerning heat transfer mechanisms and calibration of an experimental heat signal. In gas dosing experiments involving powdered catalyst samples, conduction is the predominate heat transfer mechanism. In cases where there is sufficient gas pressure in the cell headspace to enable bulk convective transfer as well, natural convection currents arise from sample heat generation during dosing, as well as from radial temperature variations within the calorimeter core when the calorimeter is maintained at temperatures above ambient. However, these currents are not strong enough to shunt significant amounts of sample-generated heat away from the thermopile sensing region. Thus, heat capture amounts do not vary with the experimental factors of catalyst bed conductivity, bed length, and gas headspace pressure.

For the simulations of gas dosing experiments where the gas headspace pressure is 10 Pa or less, radiative transfer from the catalyst bed surface to the cell headspace will shunt a significant fraction of the total sample heat emission away from the thermopile sensors unless the cell design and immediate surrounding material have downward facing walls with large view factors to capture and reflect axially radiated heat back toward the catalyst bed or toward the wall elements adjacent to the thermopile sensors. Although thermal time lags were not investigated extensively here, they are principally influenced by the thermal properties and wall thickness, and to a less extent to the thermal properties and wall thicknesses of sample, sample cell, and any wall elements that intervene between sample and the sensing thermopiles.

Acknowledgements

Financial support for this project was provided by CONACyT 35106U, and PROMEP PTC-68.

References

[1] P.C. Gravelle, Heat-flow microcalorimetry and its application to heterogeneous catalysis, Adv. Catal. 22 (1972) 191–263.
[2] P.C. Gravelle, Calorimetry in adsorption and heterogeneous catalysis studies, Catal. Rev. Sci. Eng. 16 (1977) 37–110.
[3] D.J. Parillo, R.J. Gorte, Design parameters for the construction and operation of heat-flow calorimeters, Thermochim. Acta 312 (1998) 125–132.
[4] I. Wadsö, Needs for standards in isothermal microcalorimetry, Thermochim. Acta 347 (2000) 73–77.
[5] B.E. Handy, S.B. Sharma, B.E. Spiewak, J.A. Dumesic, A Tian–Calvet heat-flux microcalorimeter for measurement of differential heats of adsorption, Meas. Sci. Technol. 4 (1993) 1350–1356.
[6] C.N. Satterfield, Heterogeneous Catalysis in Industrial Practice, 2nd ed., McGraw-Hill, New York, NY, 1990.
[7] I.G. Currie, Fundamentals Mechanics of Fluids, 2nd ed., McGraw-Hill, New York, NY, 1993.
[8] W.J. Minkowycz, E.M. Sparrow, G.E. Schneider, R.H. Pletcher, Handbook of Numerical Heat Transfer, John Wiley and Sons, New York, NY, 1988.